

Supporting Information

Spin-Electric Coupling with Anisotropy-Induced Vanishment and Enhancement in Molecular Ferroelectrics

Yu-Hui Fang [‡], Zheng Liu [‡], Shen Zhou [‡], Peng-Xiang Fu , Ye-Xin Wang ,
Zi-Yu Wang , Zhe-Ming Wang , Song Gao and Shang-Da Jiang *

* To whom correspondence should be addressed: jiangsd@scut.edu.cn

Content

SI 1. Experimental section.....	3
Synthesis and crystallization	3
EPR measurements	3
Spectrum simulation	3
SI 2. Conventional EPR study on dmaMn powder.....	4
Figure S1. CW-EPR spectrum of dmaMn powder	4
Figure S2. Pulsed EPR spectrum of dmaMn powder	5
Table S1. Spin parameters and relaxation times of dmaMn.....	6
SI 3. Conventional EPR study on aMn powder	7
Figure S3. CW-EPR spectrum of aMn powder	7
Figure S4. Pulsed EPR spectrum of aMn powder	8
Table S2. Spin parameters and relaxation times of aMn.....	9
SI 4. Spin anisotropy of aMn crystal.....	10
Figure S5. Single crystal of aMn and relationship of vectors	10
Figure S6. Single crystal structure of aMn	11
Table S3. Rotation matrix of the i -th Mn^{2+}	11
Figure S7. Angular-resolved CW-EPR spectrum of aMn at room temperature...	12
Figure S8. Angular-resolved CW-EPR spectrum of aMn at 10 K	13
SI 5. Electric-Spin Coupling Hamiltonian.....	14
SI 6. Fitting of SEC manipulation efficiency in crystal	15
Table S4. Parameters of phase evolution fitting of aMn crystal	15
Figure S9. Phase evolution fitting of five transitions	16
Figure S10. Phase evolution fitting of incremental \mathcal{E} -field.....	17
Table S5. Phase evolution fitting for incremental \mathcal{E} -field	17
Figure S11. The disappearance of spin echo evolution	17
SI 7. Fitting of SEC manipulation efficiency in powder.....	19
Table S6. Parameters of phase evolution fitting of aMn powder	19
Figure S12. Phase evolution fitting of powder samples	20
References.....	21

SI 1. Experimental section

Synthesis and crystallization

The samples were synthesized and crystallized as described in our previous work.¹⁻²

EPR measurements

Continuous-wave (CW) and pulsed EPR experiments were performed on a Bruker ElexSys E580 spectrometer, operating at the X-band ($\omega = 9.36$ GHz and $\omega = 9.70$ GHz) equipped with a goniometer for rotation and angle determination. A low-temperature environment was achieved by using an Oxford Instruments ESR900 and CF935 liquid helium cryostat.

A qualified crystal sample was attached to a sample holder in a quartz tube (Figure 1d). The rotation axis is parallel to the microwave B_1 field in the MD5 cavity. The signal of the pulsed-EPR experiments was obtained by a standard Hahn echo sequence, $\pi/2 - \tau - \pi - \tau - \text{echo}$. The echo-detected field swept (EDFS) EPR spectra were measured under variation of the static B_0 magnetic field. The T_1 values were measured by a standard inversion recovery sequence with 4-step phase cycling, $\pi - t - \pi/2 - \tau - \pi - \tau - \text{echo}$. The T_M values were determined by increasing the τ value of the standard Hahn echo sequence with 4-step phase cycling. The Rabi oscillation was measured by a nutation experiment using $t_p - t_w - \pi/2 - \tau - \pi - \tau - \text{echo}$ (where t_p is the length of the nutation pulse, $t_w > 5T_M$) as the detection sequence with 4-step phase cycling, and the Rabi frequency was determined via fast Fourier transform (FFT). The \mathcal{E} -field effect experiments were measured by inserting an increased \mathcal{E} -field pulse $t_{\mathcal{E}}$ between the $\pi/2$ and π pulses in a standard Hahn echo sequence, $\pi/2 - \tau - \pi - \tau - \text{echo}$.

Spectrum simulation

The EPR spectra were all simulated with the “EasySpin” toolbox based on MATLAB (<http://www.easyspin.org/>).³

SI 2. Conventional EPR study on dmaMn powder

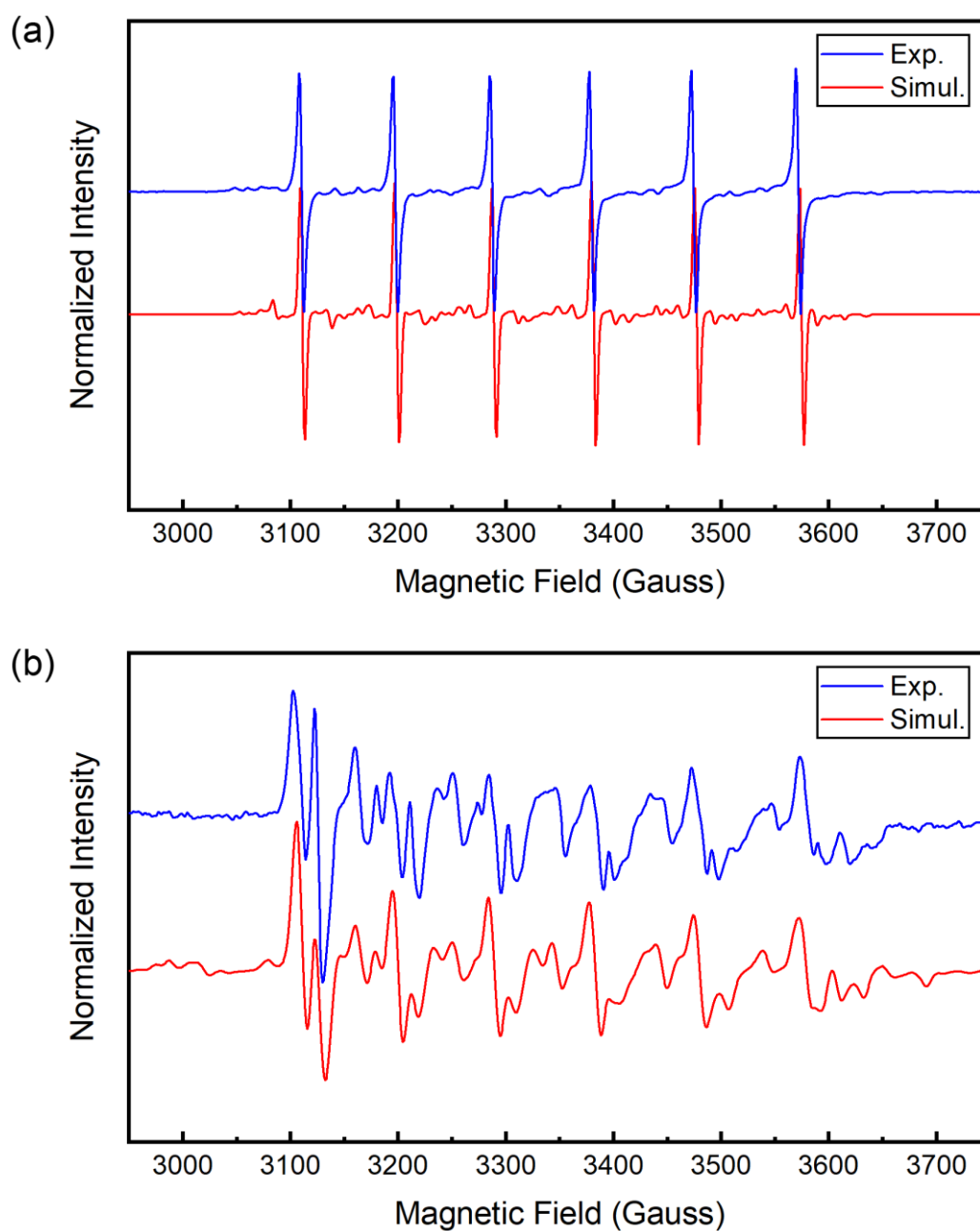


Figure S1. CW-EPR spectrum (blue) and its simulation (red) for the powder sample of dmaMn measured at (a) room temperature and (b) 10 K. The parameters are noted in Table S1.

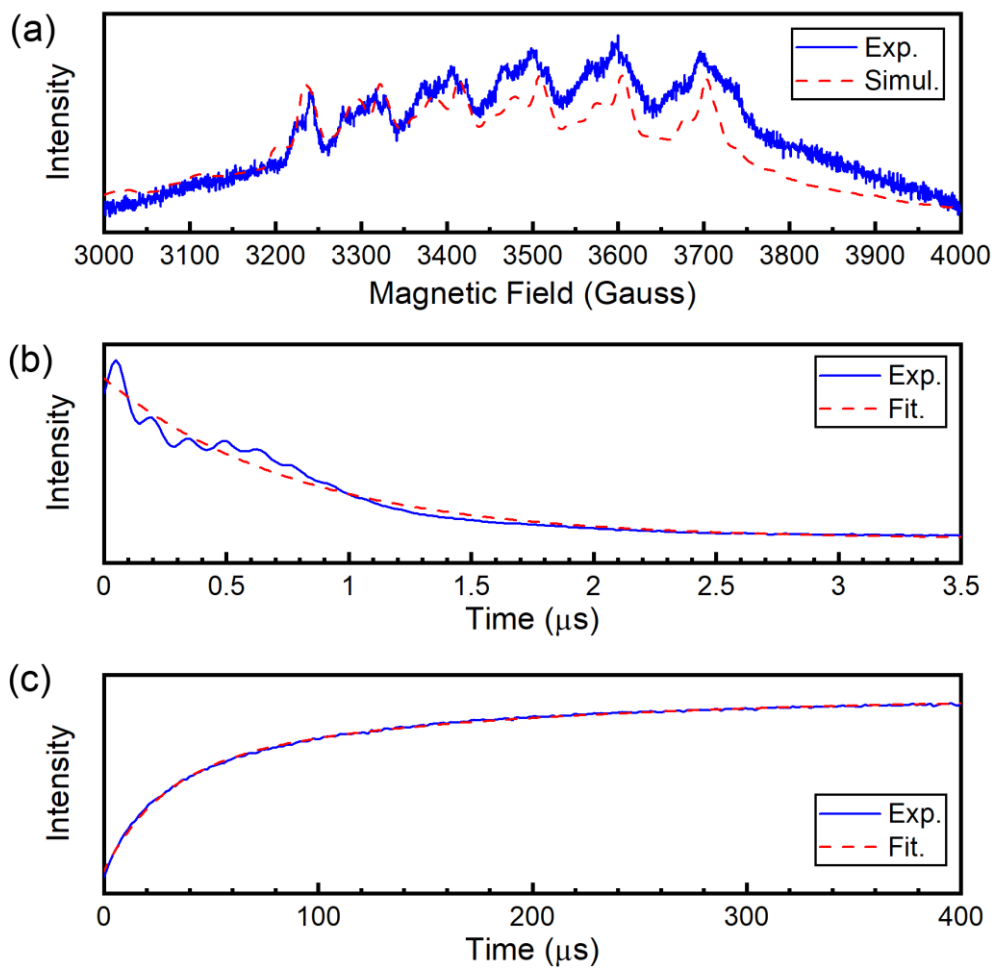


Figure S2. (a) EDFS spectrum measured at 10 K for the crystal sample of dmaMn and its simulation. (b) T_M and (c) T_1 curves measured at 3217 G and their fittings (10 K). The data are noted in Table S1.

Table S1. Parameters of CW-EPR simulation the best fits for the powder sample of dmaMn at room temperature and 10 K, and spin relaxation times at 10 K with B_0 field at 3217 G.

Room temperature		10 K	
g_{iso}	1.999	g_{iso}	2.002
$A_{\text{iso}} / \text{MHz}$	262	$A_{\text{iso}} / \text{MHz}$	262
$ D / \text{MHz}$	168	$ D / \text{MHz}$	420
E / MHz	36	E / MHz	60
Relaxation times (3217 G, 10 K)			
		T_{M} / ns	785.7
		$T_1 / \mu\text{s}$	161.7

SI 3. Conventional EPR study on aMn powder

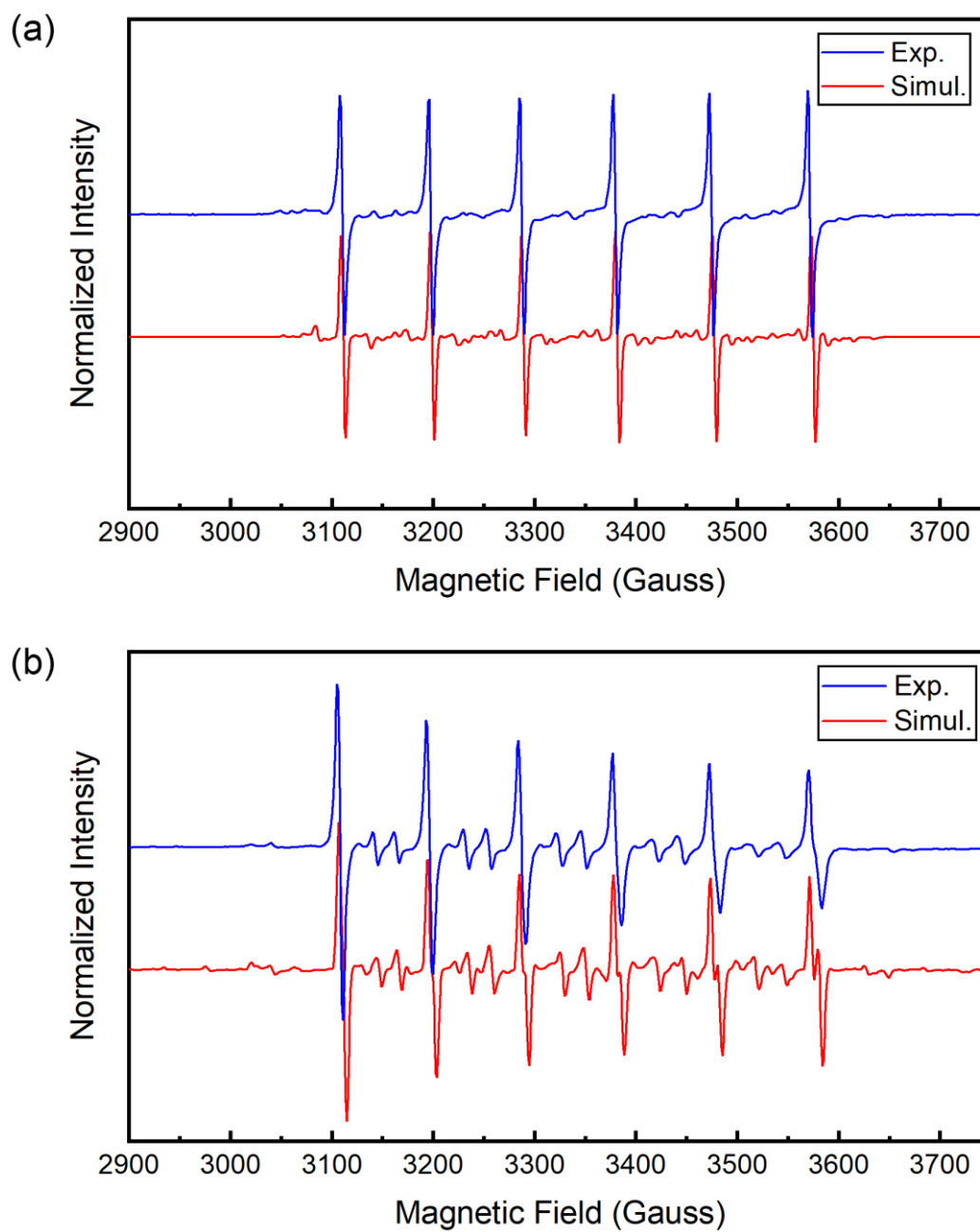


Figure S3. CW-EPR spectrum (blue) and its simulation (red) for the powder sample of aMn measured at (a) room temperature and (b) 10 K. The parameters are noted in Table S2.

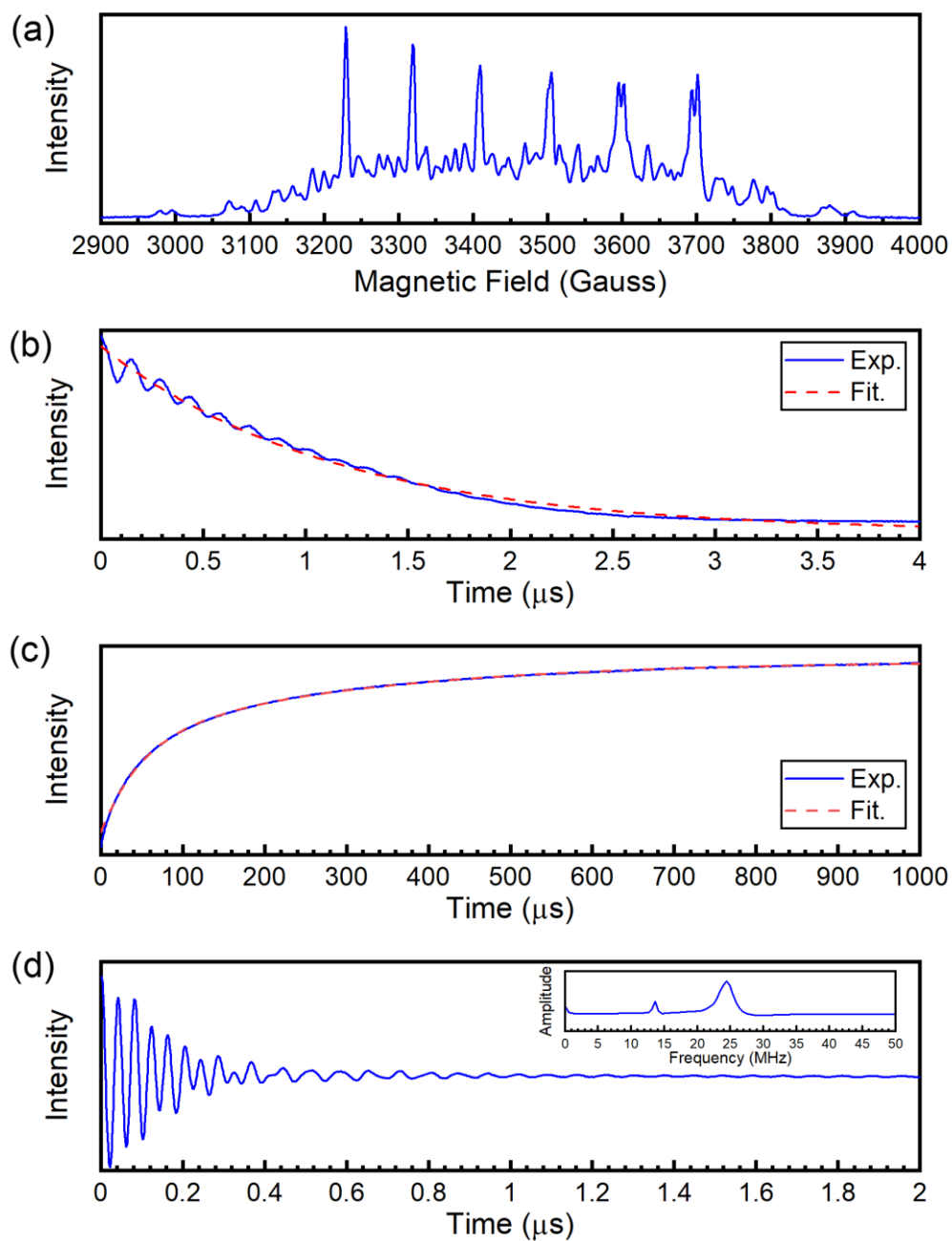


Figure S4. (a) EDFS spectrum measured at 10 K for the crystal sample of aMn. (b) T_M and (c) T_1 curves measured at 3240 G and their fittings (10 K). (d) Rabi oscillations measured at 3240 G (10 K) and its FFT result in the insert image. The data are noted in Table S2.

Table S2. Parameters of CW-EPR simulation the best fits for the powder sample of aMn at room temperature and 10 K, and spin relaxation times at 10 K with B_0 field at 3240 G.

Room temperature		10 K	
g_{iso}	1.999	g_{iso}	2.002
$A_{\text{iso}} / \text{MHz}$	263	$A_{\text{iso}} / \text{MHz}$	263
$ D / \text{MHz}$	27	$ D / \text{MHz}$	200
E / MHz	6	E / MHz	10
B_4^0 / MHz	0.06	$\theta_{\bar{c},\bar{D}} / ^\circ$	55.5
B_4^2 / MHz	1.4	Relaxation times (3240 G, 10 K)	
B_4^4 / MHz	2.4	T_M / ns	1155
$\theta_{\bar{c},\bar{D}} / ^\circ$	0	$T_1 / \mu\text{s}$	301.7
		Rabi Frequencies (3240 G, 10 K)	
		f / MHz	13.67*, 24.41

* FFT shows the Larmor precession frequency $\omega = \frac{f}{B_0} = \frac{13.67 \text{ MHz}}{0.324 \text{ T}} = 42.19 \text{ MHz/T}$, which matches the gyromagnetic ratio of ^1H $\gamma = 42.5775 \text{ MHz/T}$.

SI 4. Spin anisotropy of aMn crystal

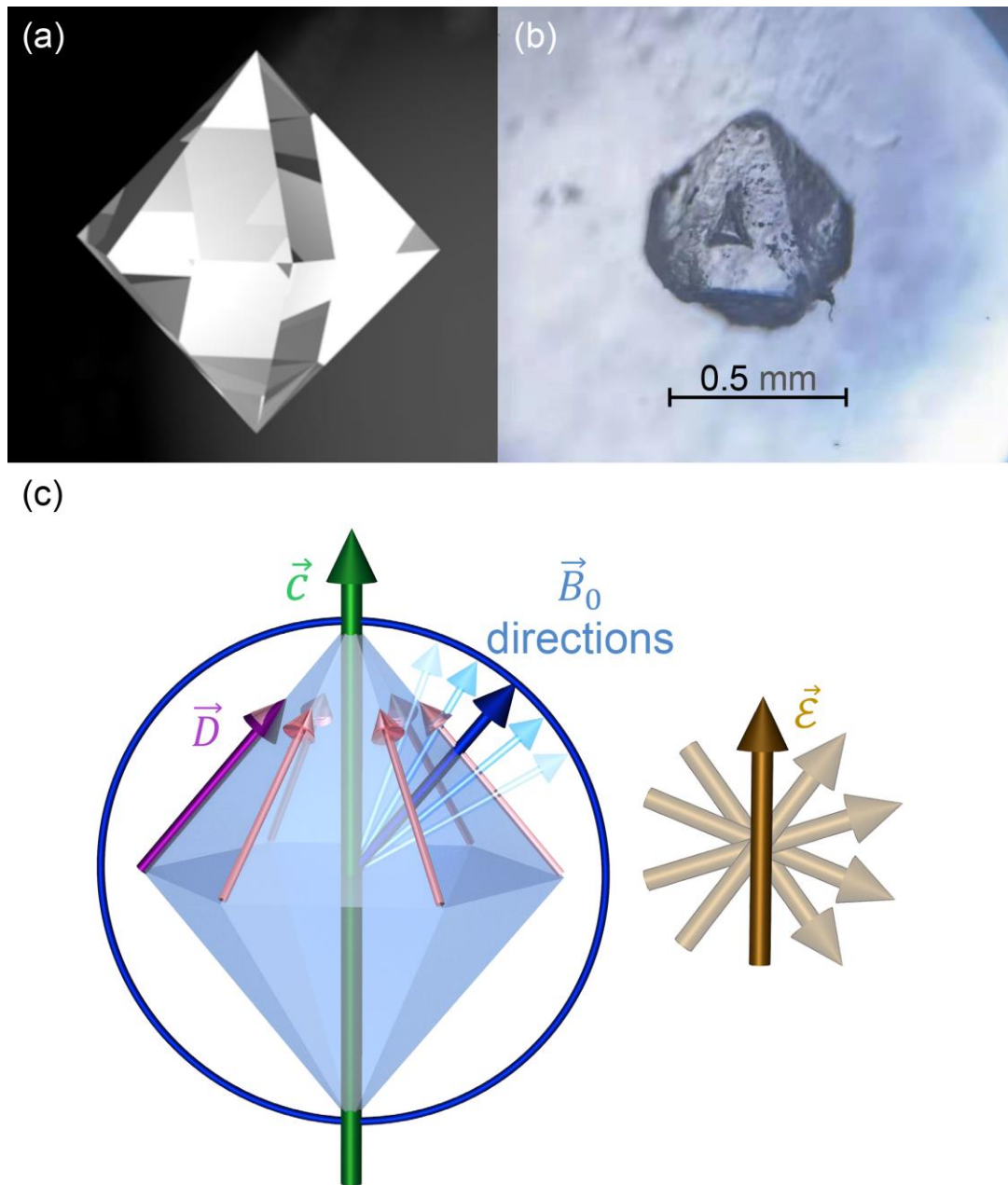


Figure S5. (a) Schematic diagram of the single crystal sample of aMn. (b) Single crystal sample of aMn under the microscope. (c) Relationships between $\theta_{\vec{c},\vec{D}}$, $\beta_{\vec{D},\vec{B}_0}$, $\beta_{\vec{c},\vec{B}_0}$, and $\beta_{\vec{c},\vec{E}}$.

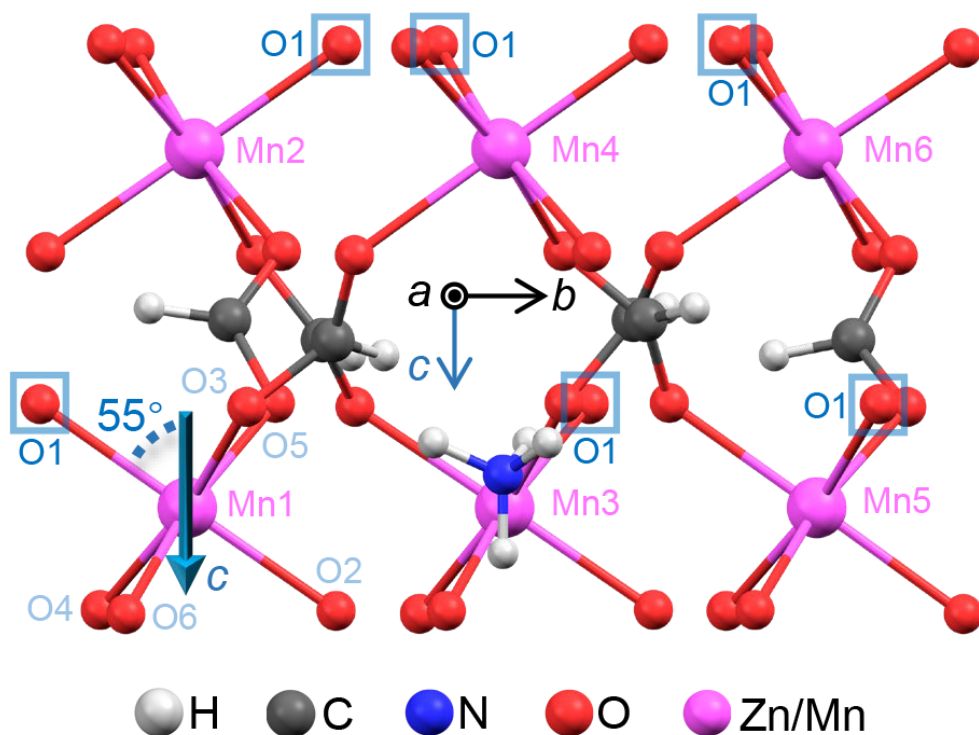


Figure S6. Single crystal structure of aMn, each Mn^{2+} is surrounded by six oxygen. The angle $\theta_{\vec{c}, \vec{d}}$ is 55.5° .¹

Table S3. Euler angles of the i -th Mn^{2+} in aMn at 10 K.

i -th Mn^{2+} ion	Euler angles
Mn1	$[0^\circ, 55.5^\circ, 0^\circ]$
Mn2	$[60^\circ, 55.5^\circ, 0^\circ]$
Mn3	$[120^\circ, 55.5^\circ, 0^\circ]$
Mn4	$[180^\circ, 55.5^\circ, 0^\circ]$
Mn5	$[240^\circ, 55.5^\circ, 0^\circ]$
Mn6	$[300^\circ, 55.5^\circ, 0^\circ]$

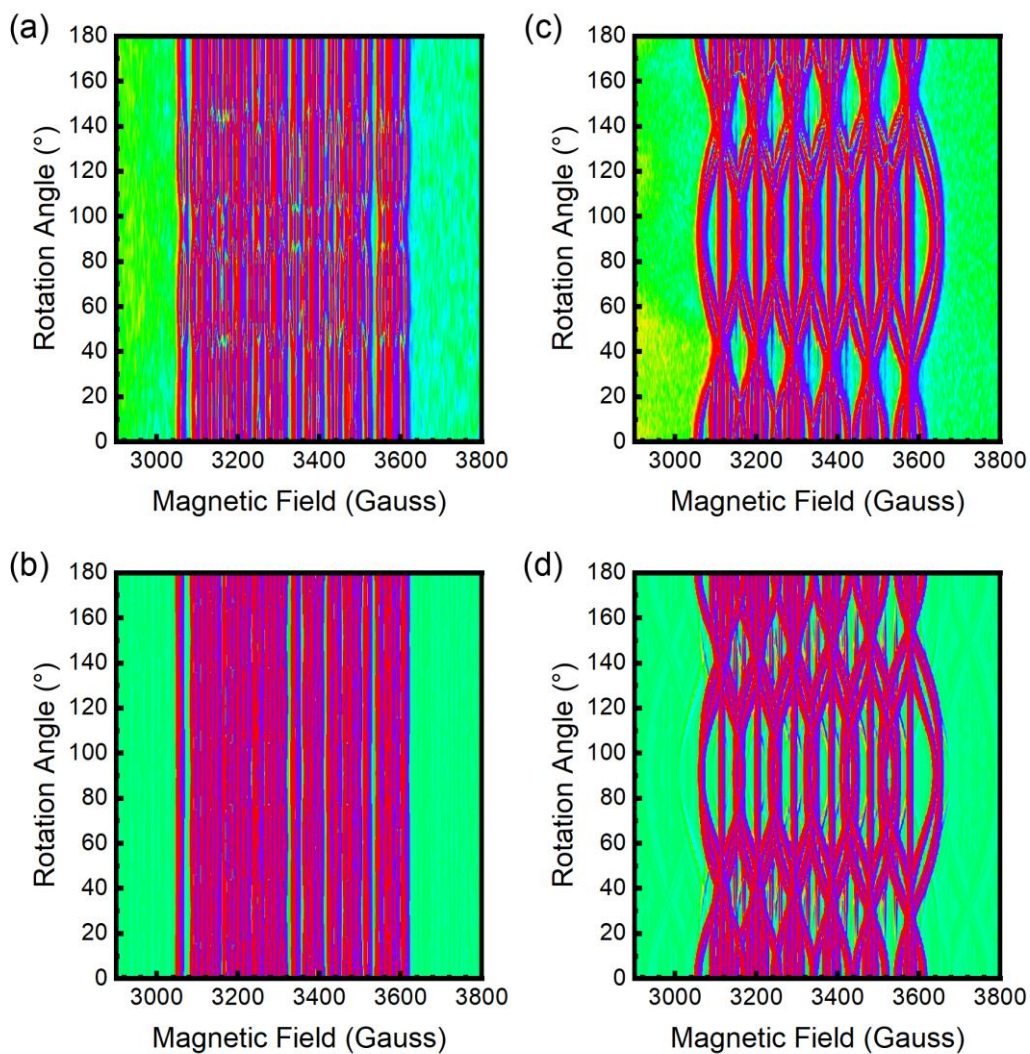


Figure S7. (a) Angular-resolved CW-EPR spectra measured at room temperature from $\beta_{\vec{a}, \vec{B}_0} = 0^\circ$ to 180° and (b) its simulation. (c) Angular-resolved CW-EPR spectra measured at room temperature from $\beta_{\vec{c}, \vec{B}_0} = 0^\circ$ to 180° and (d) its simulation. The parameters were the same with the simulation of the powder sample in Table S2.

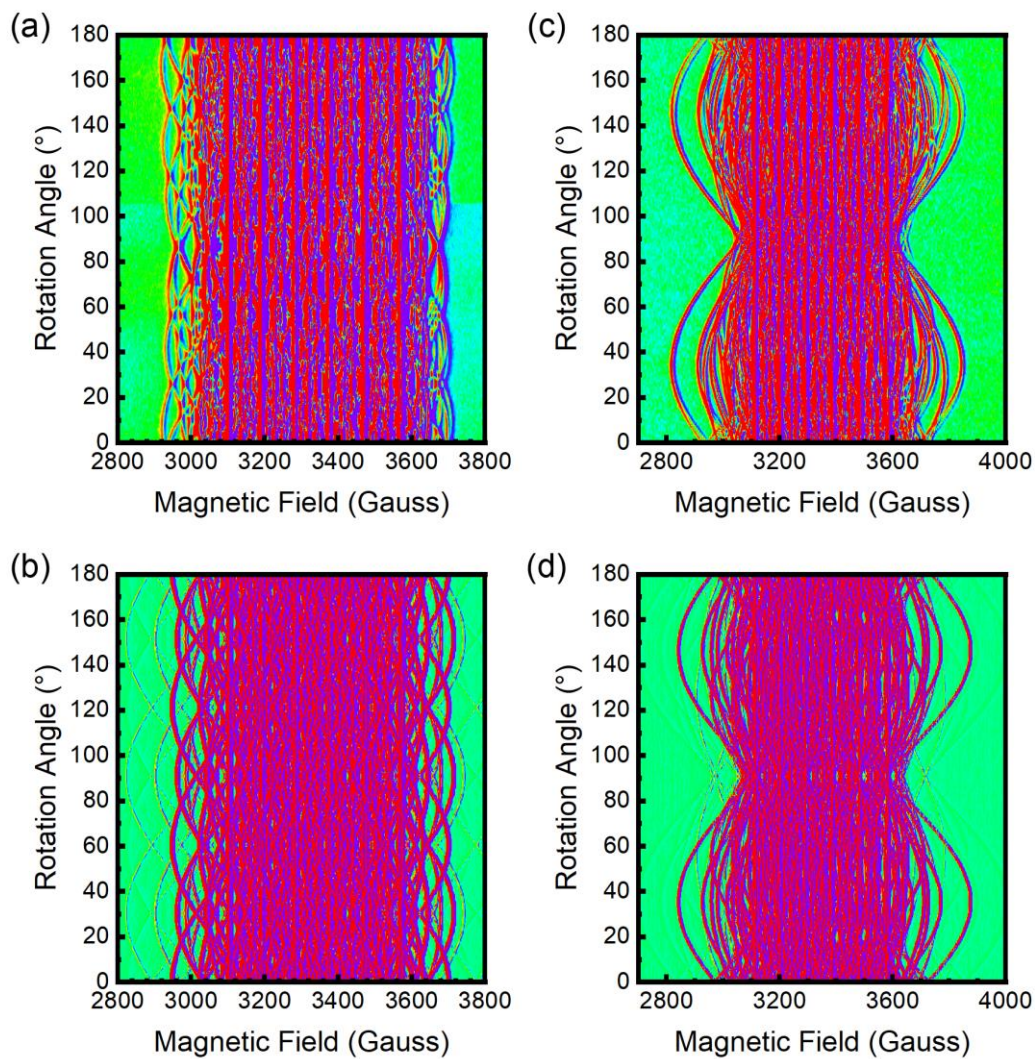


Figure S8. (a) Angular-resolved CW-EPR spectra measured at 10 K from $\beta_{\vec{a}, \vec{B}_0} = 0^\circ$ to 180° and (b) its simulation. (c) Angular-resolved CW-EPR spectra measured at 10 K from $\beta_{\vec{c}, \vec{B}_0} = 0^\circ$ to 180° and (d) its simulation. The parameters were same with the simulation of powder sample in Table S2.

SI 5. Electric-Spin Coupling Hamiltonian

Considering that the local symmetry of Mn^{2+} is C_1 in the crystal sample of aMn, the Hamiltonian of the \mathcal{E} -field can be expressed as

$$\hat{H}_{\mathcal{E}} = \hat{S}^T \left(\vec{\mathcal{E}} \cdot \frac{\partial \bar{D}}{\partial \vec{\mathcal{E}}} \right) \hat{S}$$

Considering the ferroelectricity of the crystal, only the \mathcal{E} -field component along the ferroelectricity principal axis (c-axis) affects the parameters. Hence, the effective \mathcal{E} -field strength can be expressed as

$$\mathcal{E}_{\text{eff}} = \mathcal{E} \cos \beta_{\vec{c}, \vec{\mathcal{E}}}$$

where $\beta_{\vec{c}, \vec{\mathcal{E}}}$ represents the angle between the c-axis and the applied \mathcal{E} -field.

Considering the spin Hamiltonian parameters acquired from the simulation of the CW-EPR spectra, the value of the effective ZFS (D_{eff}) can be expressed as

$$D_{\text{eff}} = \frac{3 \cos^2 \beta_{\vec{D}, \vec{B}_0} - 1}{2} |D|$$

where $\beta_{\vec{D}, \vec{B}_0}$ is the angle between the magnetic principal axis \vec{D} , and magnetic field \vec{B}_0 .

Combining the above two effective values, the Hamiltonian of the \mathcal{E} -field can be expressed as

$$\begin{aligned} \hat{H}_{\mathcal{E}} &= \hat{S}^T \left(\vec{\mathcal{E}} \cdot \frac{\partial \bar{D}}{\partial \vec{\mathcal{E}}} \right) \hat{S} \\ &= \mathcal{E}_{\text{eff}} \hat{S}^T \frac{\partial \bar{D}}{\partial \mathcal{E}_{\text{eff}}} \hat{S} \\ &= \mathcal{E}_{\text{eff}} \left(\frac{\partial D_{\text{eff}}}{\partial \mathcal{E}_{\text{eff}}} \right) \hat{S}_z^2 \\ &= \delta(D_{\text{eff}}) \hat{S}_z^2 \\ &= \mathcal{E} \cos \beta_{\vec{c}, \vec{\mathcal{E}}} \left(\frac{\partial \left(\frac{3 \cos^2 \beta_{\vec{D}, \vec{B}_0} - 1}{2} |D| \right)}{\partial \mathcal{E}_{\text{eff}}} \right) \hat{S}_z^2 \\ &= \frac{3 \cos^2 \beta_{\vec{D}, \vec{B}_0} - 1}{2} \cdot \cos \beta_{\vec{c}, \vec{\mathcal{E}}} \cdot \mathcal{E} \cdot \left(\frac{\partial |D|}{\partial \mathcal{E}_{\text{eff}}} \right) \hat{S}_z^2 \end{aligned}$$

SI 6. Fitting of SEC manipulation efficiency in crystal

Based on the preceding analysis (Eq 3), we use damped exponentially sine functions to fit the SEC manipulation efficiency of aMn crystal

$$I_{\text{im}} = \pm \sin(2\pi \cdot \nu \cdot t) \cdot e^{-\frac{t}{T}}$$

where I_{im} represents the normalized intensity of spin echoes in imaginary parts, t represents the \mathcal{E} -field time, and T represents the exponential decay factor due to the inhomogeneity of the \mathcal{E} -field. The fitting parameters are noted in Table S4, and the Fitting results were shown in Figure 4c in the main text.

Table S4. Parameters of phase evolution fitting in the xy plane for the marked transitions in Figures 4c and 4d.

Transitions	Fitting Formula	Parameters
$ +5/2\rangle \leftrightarrow +3/2\rangle$	$I_{\text{im}} = \sin(2\pi \cdot \nu_{ +5/2\rangle \leftrightarrow +3/2\rangle} \cdot t) \cdot e^{-\frac{t}{T}}$	$\nu_{ +5/2\rangle \leftrightarrow +3/2\rangle} / \mathcal{E}$ = 0.68 Hz m/V
$ +3/2\rangle \leftrightarrow +1/2\rangle$	$I_{\text{im}} = \sin(2\pi \cdot \nu_{ +3/2\rangle \leftrightarrow +1/2\rangle} \cdot t) \cdot e^{-\frac{t}{T}}$	$\nu_{ +3/2\rangle \leftrightarrow +1/2\rangle} / \mathcal{E}$ = 0.34 Hz m/V
$ +1/2\rangle \leftrightarrow -1/2\rangle$	$I_{\text{im}} = \sin(2\pi \cdot \nu_{ +1/2\rangle \leftrightarrow -1/2\rangle} \cdot t) \cdot e^{-\frac{t}{T}}$	$\nu_{ +1/2\rangle \leftrightarrow -1/2\rangle} / \mathcal{E}$ = 0 Hz m/V
$ -1/2\rangle \leftrightarrow -3/2\rangle$	$I_{\text{im}} = -\sin(2\pi \cdot \nu_{ -1/2\rangle \leftrightarrow -3/2\rangle} \cdot t) \cdot e^{-\frac{t}{T}}$	$\nu_{ -1/2\rangle \leftrightarrow -3/2\rangle} / \mathcal{E}$ = 0 Hz m/V
$ -3/2\rangle \leftrightarrow -5/2\rangle$	$I_{\text{im}} = -\sin(2\pi \cdot \nu_{ -3/2\rangle \leftrightarrow -5/2\rangle} \cdot t) \cdot e^{-\frac{t}{T}}$	$T = 3.57 \mu\text{s}$

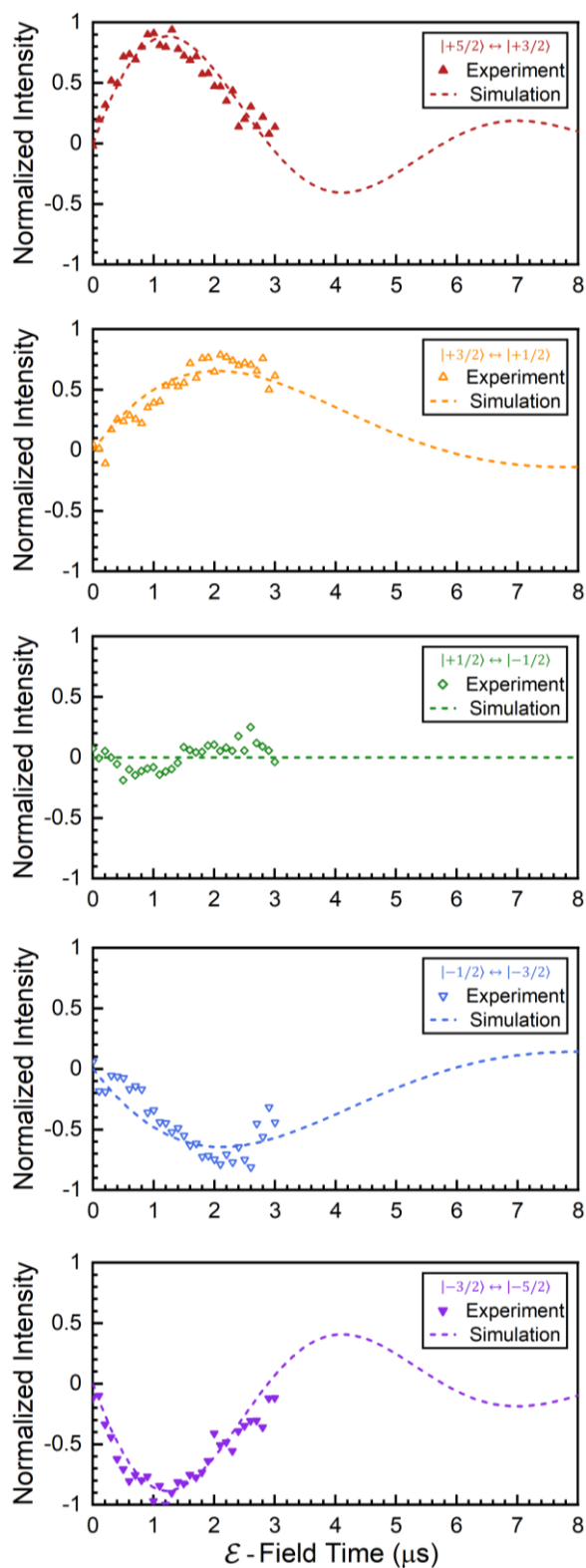


Figure S9. Imaginary parts of echoes of five transitions noted in Table S4 and their fittings with damped exponential sine functions.

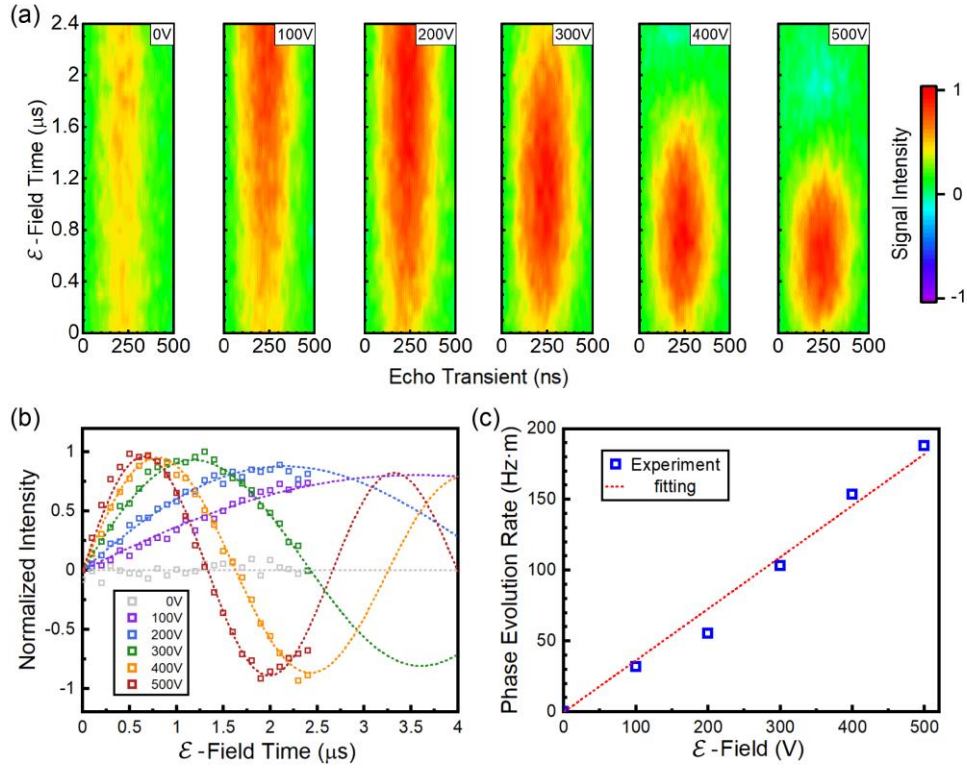


Figure S10. (a) Imaginary parts of echoes at 3212 G of incremental \mathcal{E} -field noted in Table S5 and (b) their fitting results with damped exponential functions. (c) Linear fitting of phase revolution rate versus incremental \mathcal{E} -field.

Table S5. Parameters of phase evolution fitting in the xy plane for incremental \mathcal{E} -field in Figures S10.

\mathcal{E} -field strength	Fitting Formula	Parameters
0 V	$I_{\text{im}} = \sin(2\pi \cdot \nu_{0\text{V}} \cdot t) \cdot e^{-\frac{t}{T}}$	$\nu_{0\text{V}} = 0 \text{ Hz} \cdot \text{m}$
100 V	$I_{\text{im}} = \sin(2\pi \cdot \nu_{100\text{V}} \cdot t) \cdot e^{-\frac{t}{T}}$	$\nu_{100\text{V}} = 31.8 \text{ Hz} \cdot \text{m}$
200 V	$I_{\text{im}} = \sin(2\pi \cdot \nu_{200\text{V}} \cdot t) \cdot e^{-\frac{t}{T}}$	$\nu_{200\text{V}} = 55.2 \text{ Hz} \cdot \text{m}$
300 V	$I_{\text{im}} = \sin(2\pi \cdot \nu_{300\text{V}} \cdot t) \cdot e^{-\frac{t}{T}}$	$\nu_{300\text{V}} = 103 \text{ Hz} \cdot \text{m}$
400 V	$I_{\text{im}} = \sin(2\pi \cdot \nu_{400\text{V}} \cdot t) \cdot e^{-\frac{t}{T}}$	$\nu_{400\text{V}} = 153 \text{ Hz} \cdot \text{m}$
500 V	$I_{\text{im}} = \sin(2\pi \cdot \nu_{500\text{V}} \cdot t) \cdot e^{-\frac{t}{T}}$	$\nu_{500\text{V}} = 188 \text{ Hz} \cdot \text{m}$
		$T = 17.2 \mu\text{s}$

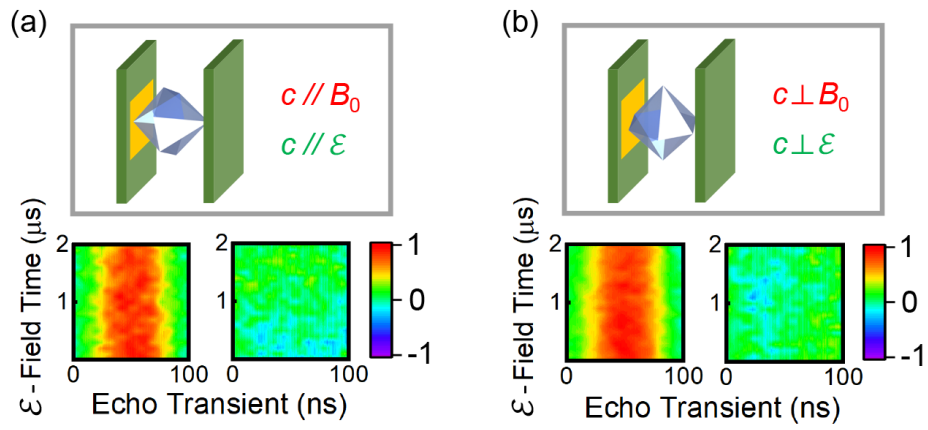


Figure S11. (a, b) The disappearance of spin echo evolution with \mathcal{E} -field on a single crystal sample of aMn at 10 K, when the c -axis is (a) parallel and (b) perpendicular to the magnetic field and \mathcal{E} -field.

SI 7. Fitting of SEC manipulation efficiency in powder

For powder samples, it is also necessary to consider the different magnetic and \mathcal{E} - fields felt by the disordered molecular orientation. Considering the relationship between the spin phase evolution ($\Delta\phi$) and the Hamiltonian of the \mathcal{E} -field effect,

$$\Delta\phi = 2\pi \cdot \nu \cdot t$$

$$\hat{H}_{\mathcal{E}} = \frac{3 \cos^2 \beta_{\vec{D}, \vec{B}_0} - 1}{2} \cos \beta_{\vec{c}, \vec{\mathcal{E}}} \mathcal{E} \left(\frac{\partial |D|}{\partial \mathcal{E}_{\text{eff}}} \right) \hat{S}_z^2$$

For a single Mn^{2+} ion with a specific orientation, its normalized spin echo intensity can be expressed as

$$\begin{aligned} I_{\text{single}} &= \cos(\Delta\phi) = \cos(2\pi \cdot \nu_{\text{powder}} \cdot t) \\ &= \cos \left(2\pi \cdot \left(\frac{3 \cos^2 \beta_{\vec{D}, \vec{B}_0} - 1}{2} \cos \beta_{\vec{c}, \vec{\mathcal{E}}} \mathcal{E} \left(\frac{\partial |D|}{\partial \mathcal{E}_{\text{eff}}} \right) \hat{S}_z^2 \right) \cdot t \right) \\ &= \cos \left(2\pi \cdot \left(\frac{3(\sin\alpha_1 \cos\alpha_2 \sin 55.5^\circ + \cos\alpha_1 \cos 55.5^\circ)^2 - 1}{2} \cos\alpha_1 \mathcal{E} \left(\frac{\partial |D|}{\partial \mathcal{E}_{\text{eff}}} \right) \hat{S}_z^2 \right) \cdot t \right) \end{aligned}$$

where α_1 and α_2 are the polar angle and azimuthal angle of the external fields respect to the molecular frame in Figure S5. $\left(\frac{\partial |D|}{\partial \mathcal{E}_{\text{eff}}} \right)$ is the manipulation efficiency to be fit in the powder samples.

Integrating the random distribution of the sample in a sphere space with the spin echo intensity of the ensemble can be obtained by

$$I_{\text{ensemble}} = e^{-\frac{t}{T}} \iint I_{\text{single}} d\alpha_1, \alpha_2$$

where $e^{-\frac{t}{T}}$ represents the exponential decay term due to the inhomogeneity of the \mathcal{E} -field.

Table S6. Parameters of phase evolution fitting in Figure 1f.

Powder Samples	Parameters
dmaMn	$\nu_{\text{dmaMn}}/\mathcal{E} = 0.10 \text{ Hz} \cdot \text{m/V}$ $T_{\text{dmaMn}} = 1.5 \mu\text{s}$
aMn	$\nu_{\text{aMn}}/\mathcal{E} = 0.34 \text{ Hz} \cdot \text{m/V}$ $T_{\text{aMn}} = 0.65 \mu\text{s}$

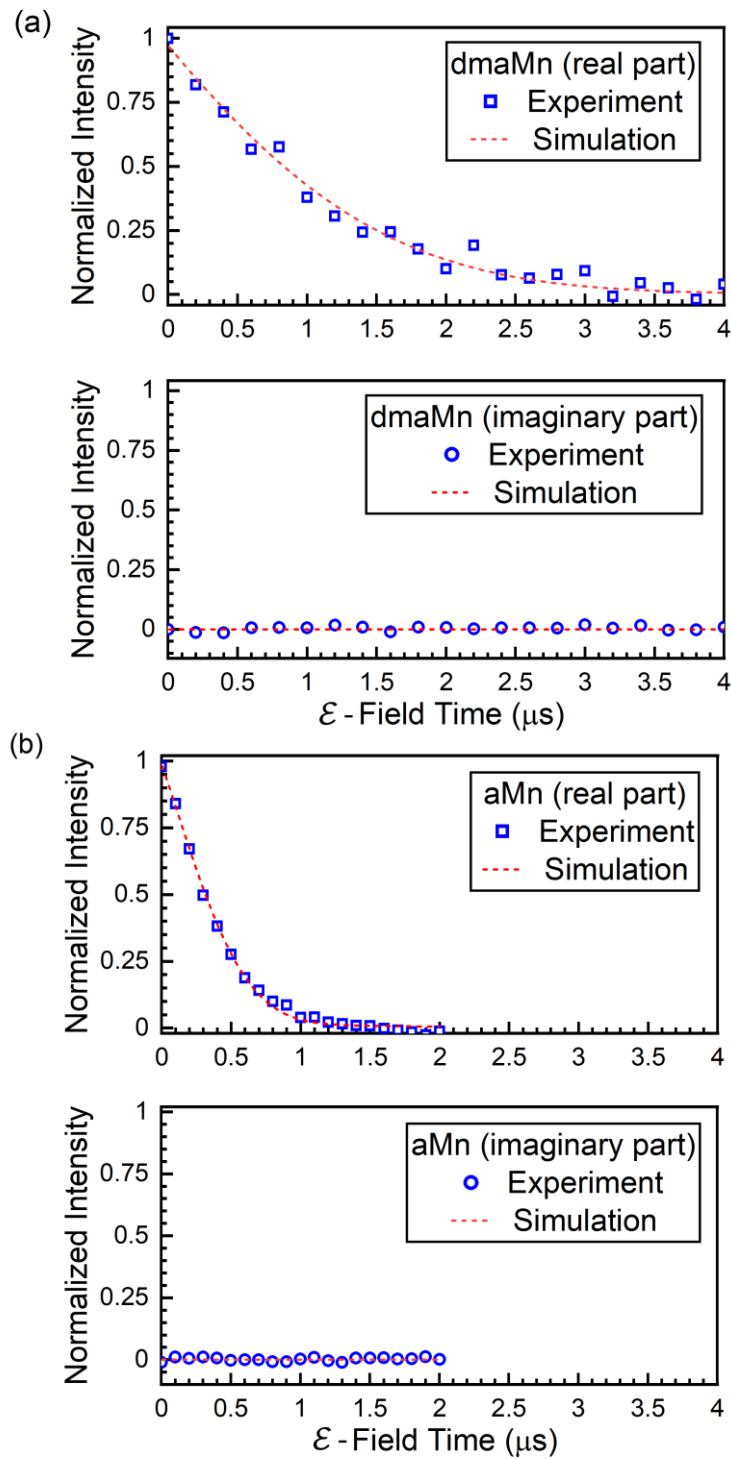


Figure S12. (a) Integral spin echo intensities of dmaMn in Figure 1e and their fitting results (dotted lines) noted in Table S5. (b) Integral spin echo intensities of aMn in Figure 1e and their fitting results (dotted lines) noted in Table S5.

References

- (1) Xu, G.; Ma, X.; Zhang, L.; Wang, Z.; Gao, S., Disorder—Order Ferroelectric Transition in the Metal Formate Framework of $[\text{NH}_4][\text{Zn}(\text{HCOO})_3]$. *J. Am. Chem. Soc.* **2010**, *132* (28), 9588-9590.
- (2) Wang, X.-Y.; Gan, L.; Zhang, S.-W.; Gao, S., Perovskite-like Metal Formates with Weak Ferromagnetism and as Precursors to Amorphous Materials. *Inorg. Chem.* **2004**, *43* (15), 4615-4625.
- (3) Stoll, S.; Schweiger, A., EasySpin, a comprehensive software package for spectral simulation and analysis in EPR. *J. Magn. Reson.* **2006**, *178* (1), 42-55.